

1 **Title**

2 Thalamic Roles in Conscious Perception Revealed by Low-Intensity Focused Ultrasound  
3 Neuromodulation

4

5 **Author list**

6 Hyunwoo Jang<sup>1,2</sup>, Panagiotis Fotiadis<sup>2,3</sup>, George A. Mashour<sup>1,2,3,4,5</sup>, Anthony G. Hudetz<sup>1,2,3,4</sup>,  
7 Zirui Huang<sup>1,2,3,4,\*</sup>

8

9 **Affiliations**

10 <sup>1</sup> Neuroscience Graduate Program, University of Michigan, Ann Arbor, MI 48109, USA

11 <sup>2</sup> Center for Consciousness Science, University of Michigan Medical School, Ann Arbor, MI 48109, USA

12 <sup>3</sup> Department of Anesthesiology, University of Michigan Medical School, Ann Arbor, MI 48109, USA

13 <sup>4</sup> Michigan Psychedelic Center, University of Michigan Medical School, Ann Arbor, MI, 48109, USA

14 <sup>5</sup> Department of Pharmacology, University of Michigan Medical School, Ann Arbor, MI, 48109, USA

15 \* Correspondence and requests for materials should be addressed to Z.H.

16 (Email: [huangzu@med.umich.edu](mailto:huangzu@med.umich.edu))

17

18 **ABSTRACT**

19 The neural basis of conscious perception remains incompletely understood. While cortical  
20 mechanisms of conscious content have been extensively investigated, the role of subcortical  
21 structures, including the thalamus, remains less explored. We aim to elucidate the causal  
22 contributions of different thalamic regions to conscious perception using transcranial low-intensity  
23 focused ultrasound (LIFU) neuromodulation. We hypothesize that modulating different thalamic  
24 regions would result in distinct perceptual outcomes. We apply LIFU in human volunteers to  
25 investigate region-specific and sonication parameter-dependent effects. We target anterior  
26 (transmodal-dominant) and posterior (unimodal-dominant) thalamic regions, further divided into  
27 ventral and dorsal regions, while participants perform a near-threshold visual perception task.  
28 Task performance is evaluated using Signal Detection Theory metrics. We find that the high duty  
29 cycle stimulation of the ventral anterior thalamus enhanced object recognition sensitivity. We also  
30 observe a general (i.e., region-independent) effect of LIFU on decision bias (i.e., a tendency  
31 toward a particular response) and object categorization accuracy. Specifically, high duty cycle  
32 stimulation decreases categorization accuracy, whereas low duty cycle shifts decision bias  
33 towards a more conservative stance. In conclusion, our results provide causal insight into the  
34 functional organization of the thalamus in shaping human visual experience and highlight the  
35 unique role of the transmodal-dominant ventral anterior thalamus.

36

37

## 38 INTRODUCTION

39 The neural basis of conscious perception remains an active area of neuroscientific investigation<sup>1–</sup>  
40 <sup>7</sup>. While cortical mechanisms of conscious contents have been extensively studied<sup>8–12</sup>, the role of  
41 subcortical structures in enabling or modulating such contents remains less explored<sup>13</sup>. With its  
42 intricate connections to the cortex, the thalamus is a central structure that may mediate conscious  
43 experience<sup>14–17</sup>. Traditionally, thalamic nuclei have been categorized into specific and nonspecific  
44 types. Specific nuclei relay modal sensory information to designated cortical areas, whereas  
45 nonspecific nuclei project more broadly, regulating cortical arousal and supporting higher-order  
46 cognition<sup>16,18,19</sup>. For instance, the lateral geniculate nucleus (specific) relays retinal input to the  
47 primary visual cortex<sup>20</sup>, while the intralaminar thalamus (nonspecific) are involved in controlling  
48 arousal, attention, and state of consciousness<sup>21–23</sup>.

49 Recent research suggests a continuum rather than distinct categories of cortical and thalamic  
50 areas<sup>24,25</sup>. In the cortex, unimodal areas process sensorimotor information received from the  
51 environment, while transmodal areas further integrate this information, fostering more complex  
52 cognition<sup>26–28</sup>. Building on this functional organization of the cortex, our previous work revealed a  
53 unimodal-transmodal gradient in thalamocortical connectivity<sup>29</sup>. This thalamic functional gradient  
54 is characterized by a predominance of connectivity between the posterior thalamus and unimodal  
55 cortices, and a predominance of connectivity between the anterior/medial thalamus and  
56 transmodal cortices. This connectivity gradient also corresponds to the underlying  
57 cytoarchitecture of the thalamus, where core cells are concentrated in posterior regions and  
58 diffusely projecting matrix cells are enriched anteriorly<sup>29,30</sup>. Notably, research has implicated  
59 matrix cells as being crucial for conscious sensory processing<sup>1,10,22,31–37</sup>, where a disruption of  
60 matrix-rich thalamic areas has been linked to loss of consciousness<sup>29</sup>. Therefore, understanding  
61 these functional and structural gradients within the thalamus is critical for elucidating the neural  
62 mechanisms underlying conscious perception.

63 To causally probe thalamic roles in conscious perception, precise stimulation of deep brain areas  
64 is essential. Traditional methods such as deep-brain stimulation, optogenetics, and transcranial  
65 electrical stimulation are either invasive or lack spatial resolution<sup>38,39</sup>. Instead, transcranial low-  
66 intensity focused ultrasound (LIFU) provides a non-invasive and precise way to target deep  
67 structures<sup>40–46</sup>. Although the exact mechanisms behind LIFU's effects are still being explored—  
68 with hypotheses ranging from thermal effects<sup>47</sup> to membrane pore formation<sup>48</sup> and  
69 mechanosensitive channel activation<sup>49</sup>—its effectiveness in modulating neural activity and  
70 behavior has been well-established<sup>40,48,50–52</sup>. However, its impact on conscious perception  
71 remains largely uncharted territory. Notably, the effects of LIFU are known to be influenced by  
72 parameters such as duty cycle (i.e., the percentage of time the ultrasound is actively transmitting  
73 within each pulse cycle). High duty cycles generally lead to excitation and low duty cycles to  
74 inhibition<sup>48,49,53</sup>. Yet, the optimal sonication parameters for modulating perception—particularly in  
75 human subcortex—are still to be determined.

76 In this work, we aim to elucidate the causal roles of thalamic regions in conscious perception,  
77 hypothesizing that sonicating different regions or applying different stimulation parameters (i.e.,  
78 duty cycle) will lead to distinct perceptual outcomes. We specifically apply LIFU in healthy  
79 volunteers while they are performing a near-threshold visual task and evaluate changes in their  
80 visual perception using metrics derived from Signal Detection Theory (SDT). For this purpose, we  
81 sequentially stimulate four thalamic areas (ventral anterior/posterior and dorsal anterior/posterior).

82 Our findings reveal that the transmodal-dominant ventral anterior thalamus significantly  
83 modulates the sensitivity of conscious visual perception. Additionally, we demonstrate both  
84 common (region-independent) and duty cycle-dependent effects of LIFU on decision bias and  
85 categorization accuracy in object recognition.

86

## 87 RESULTS

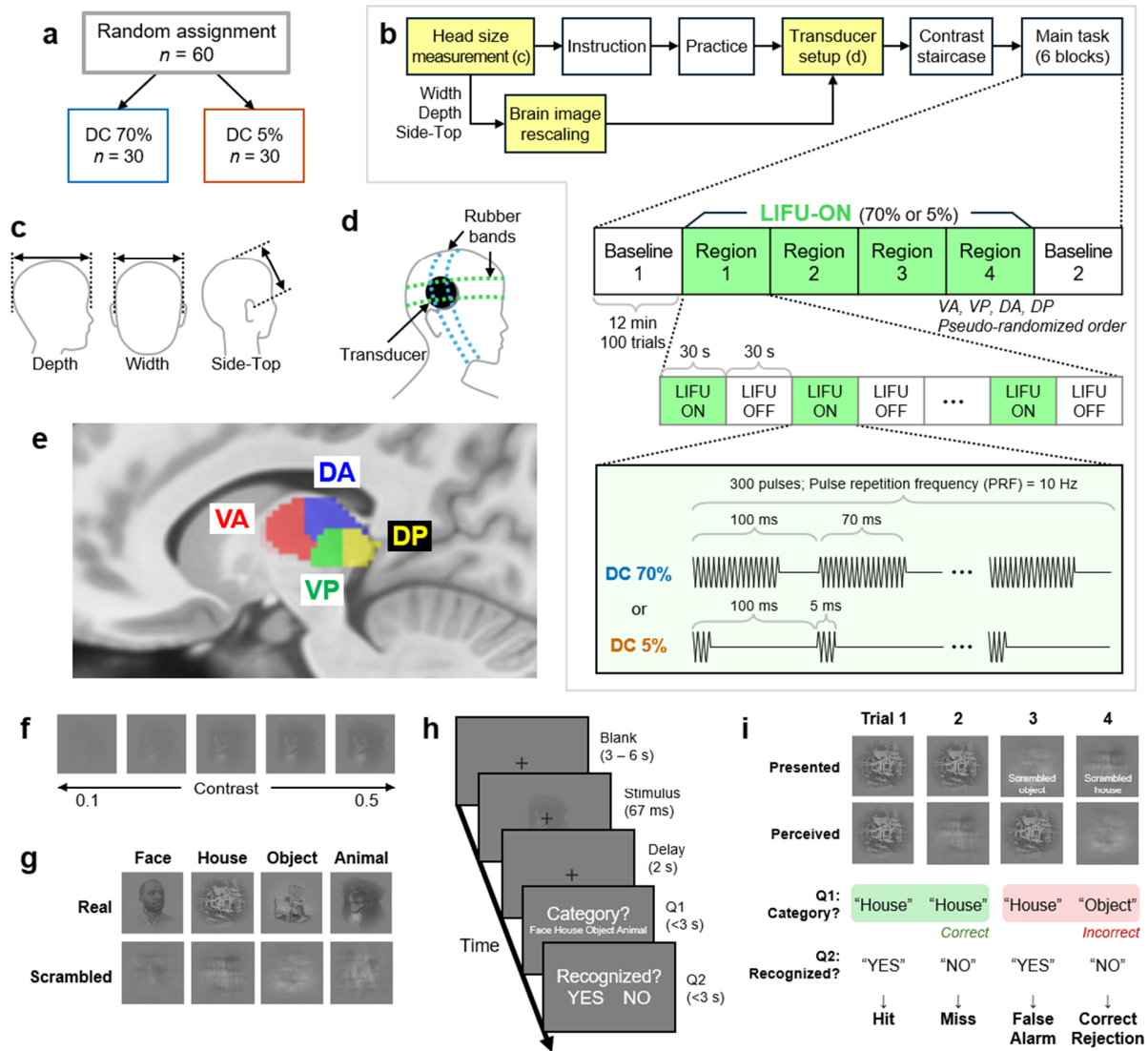
88 Sixty participants (age:  $25.9 \pm 6.3$ , mean  $\pm$  SD; 38 females, 22 males) were randomly assigned  
89 to one of the two duty cycle groups. One group received LIFU with a high duty cycle (70%), while  
90 the other received LIFU with a low duty cycle (5%) with equal spatial-peak temporal-average  
91 intensity of  $I_{spta} = 0.72 \text{ W cm}^{-2}$  (Fig. 1a). The experiment involved several key steps, such as  
92 transducer setup, image contrast titration, and six blocks of the visual task (Fig. 1b-d). There were  
93 two outer LIFU-OFF baseline blocks (Baseline-1 and Baseline-2) and four inner LIFU-ON blocks.  
94 During each LIFU-ON block, LIFU was administered to only one of four regions of the left thalamus,  
95 including the ventral anterior (VA), ventral posterior (VP), dorsal anterior (DA), and dorsal  
96 posterior (DP) thalamus (Fig. 1e). The order of stimulated regions was pseudo-randomized and  
97 counterbalanced among participants, and each participant received a consistent duty cycle  
98 throughout the session. By including multiple targets, we could analyze in within-subject manner  
99 as a function of stimulated region.

100 We employed a well-established near-threshold visual object recognition and categorization  
101 task<sup>8,9</sup>. Stimuli were presented at the intensity close to the threshold of conscious perception.  
102 Using an adaptive staircase paradigm, we titrated the image contrast for each participant<sup>8,54</sup> (Fig.  
103 1f). Four object categories were used: faces, houses, human-made objects, and animals (Fig. 1g).  
104 We also included scrambled images, which comprised 20 out of 100 trials. During each trial,  
105 participants responded to two questions: one regarding the category of the presented image (i.e.,  
106 “What category did the observed image belong to?”) and another concerning their subjective  
107 recognition experience (i.e., “Did you have a meaningful visual experience?”) (Fig. 1h). Here,  
108 ‘recognition’ was operationally defined as the perception of an object that makes sense in the real  
109 world, as opposed to meaningless noise-like patterns. Therefore, the recognition rates for real  
110 and scrambled images could be interpreted as hits and false alarms, respectively (Fig. 1i).

111 Based on hit and false alarm rates, we evaluated sensitivity and decision bias for object  
112 recognition within the SDT framework (see Methods: Signal detection theory analysis). Sensitivity  
113 reflects the ability to differentiate between real and scrambled images, while decision bias  
114 indicates a tendency towards a particular response. Herein, a high bias signifies a tendency to  
115 say “NO” (i.e., “Didn’t have a meaningful visual experience”) to the recognition question  
116 (Question-2), reflecting a conservative stance in object recognition. Categorization accuracy was  
117 also quantified, independently of object recognition.

118 During Baseline-1, participants recognized  $54.7 \pm 14.7\%$  (mean  $\pm$  SD) of the real images  
119 (Supplementary Fig. 1a), which was not significantly different from the intended 50% recognition  
120 rate, confirming the successful implementation of the staircase procedure (see SI text and  
121 Supplementary Fig. 1 for statistics and additional analyses on baseline perceptual outcomes). We  
122 also found no significant differences in perceptual outcomes between the two baselines,  
123 suggesting that LIFU did not produce detectable long-lasting effects within our experimental  
124 timescale of approximately one hour (Supplementary Fig. 2).

125



126

127 **Fig. 1: Overview of the block design, experimental setup, and behavioral paradigm.** **a** Randomized  
 128 study group assignment. Sixty subjects were randomly assigned to one of two groups, each consisting of  
 129 30 participants, corresponding to either a 70% or 5% duty cycle (DC). **b** The timeline of experimental  
 130 sessions, including initial preparation steps and the main task. The main task included two baseline blocks  
 131 and four LIFU-ON blocks with a pseudo-randomized order of stimulation regions. Each block comprised  
 132 100 trials. Each LIFU-ON block included 12 alternating 30-second ON and OFF epochs, with each ON  
 133 epoch consisting of 300 pulses of varying duty cycles (pulse repetition frequency = 10 Hz). **c** Measurement  
 134 locations for head size, including width, depth, and side-to-top. **d** Illustration of the transducer fixed with two  
 135 perpendicular rubber bands on the participant's head. **e** Sagittal view for the four subdivisions of the left  
 136 thalamus: ventral anterior (VA), ventral posterior (VP), dorsal anterior (DA), and dorsal posterior (DP)  
 137 thalamus, overlaid on standard MNI template brain images. **f** Example of an animal image displayed at  
 138 different contrast levels. **g** Examples of real and scrambled images for each category (face, house, human-  
 139 made object, and animal). **h** Trial structure showing the sequence of events: a blank period, stimulus  
 140 presentation, delay, and two questions (categorization and recognition). **i** Illustration of the four trial types  
 141 (hit, miss, false alarm, and correct rejection). Due to copyright limitations, the actual images used in our

142 experiment are not shown. Copyright-free images included in this figure were obtained from  
143 <https://www.pexels.com>.

144

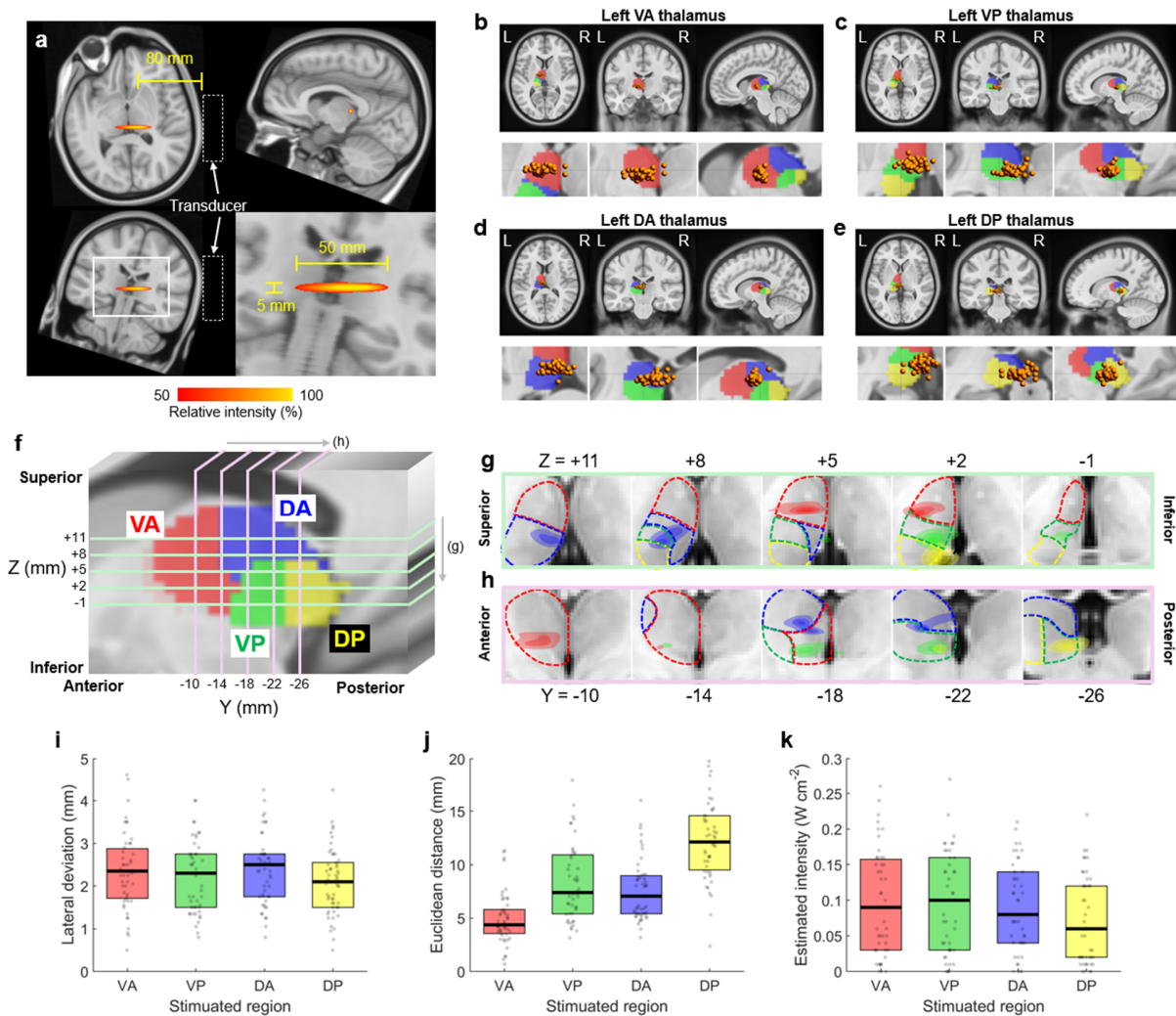
### 145 **Ultrasound beam profile and targeting accuracy**

146 We simulated the LIFU beam *in silico* on an MNI template brain to characterize the beam profile  
147 (Fig. 2a). The beam exhibited a bullet-like shape with an aspect ratio of approximately 10,  
148 measuring 50 mm in length and 5 mm in width, in agreement with a previous study which used  
149 the identical transducer<sup>55</sup>. The location of peak intensity was observed at 80 mm, consistent with  
150 the device specifications. The temperature increase in the brain tissue was minimal, with a  
151 maximum recorded rise of 0.15°C (Supplementary Fig. 3).

152 As proof of concept, we utilized the MNI template brain image as a pseudo-anatomical reference  
153 for the stimulation procedure (see Methods for details) by rescaling the MNI template image to  
154 match each participant's head size. We independently validated the accuracy of this method by  
155 comparing the actual anatomical images and the rescaled images extracted from five individuals,  
156 confirming an average deviation of  $1.7 \pm 0.6$  mm (Supplementary Fig. 4).

157 Post-hoc analysis confirmed successful targeting of each thalamic region (Fig. 2b-h). Probability  
158 density maps showed distinct targeting with minimal overlap (Fig. 2g,h). Mean lateral deviation  
159 (i.e., the distance from the target to the actual beam center, viewed from an angle perpendicular  
160 to the beam) was consistent across regions ( $2.3 \pm 0.9$  mm; Fig. 2i), validating region-level LIFU  
161 targeting. The Euclidean distance of the focal center from the target was  $8.3 \pm 4.1$  mm,  
162 comparable to previous studies (Fig. 2j)<sup>55</sup>. Under the intensity setting of  $I_{spta} = 0.72$  W cm<sup>-2</sup>, the  
163 simulated intensity at the beam center was estimated to be  $0.09 \pm 0.07$  W cm<sup>-2</sup> ( $87.7 \pm 9.0\%$   
164 energy loss; Fig. 2k).

165



166

167 **Fig. 2: LIFU beam profiles and targeting accuracy.** **a** Geometrical profile of the LIFU beam simulated on  
 168 the MNI template brain, with the transducer placed on the right temple. **b-e** Estimated beam centers in the  
 169 left thalamus for each region: **b** VA, **c** VP, **d** DA, and **e** DP thalamus. VA:  $n = 51$ ; VP:  $n = 50$ ; DA:  $n = 53$ ;  
 170 DP:  $n = 54$ . Orange spheres indicate the estimated centers of the LIFU beams. The bottom images are  
 171 zoomed-in views. **f** Sagittal view of the thalamus with the y and z coordinates of the cross-sections in MNI  
 172 space. **g, h** Cross-sectional views displaying the probability density functions of the sonication centers for  
 173 each thalamic region in the **g** x-y and **h** x-z planes. **i** Lateral deviation of beam centers from the  
 174 corresponding target. VA:  $n = 51$ ; VP:  $n = 50$ ; DA:  $n = 53$ ; DP:  $n = 54$ . **j** Euclidean distance of beam centers  
 175 from the corresponding target. VA:  $n = 50$ ; VP:  $n = 48$ ; DA:  $n = 51$ ; DP:  $n = 51$ . **k** Estimated temporal  
 176 intensity at the beam centers. VA:  $n = 47$ ; VP:  $n = 46$ ; DA:  $n = 46$ ; DP:  $n = 47$ . Box plots show the median,  
 177 upper, and lower quartiles. Color coding for the thalamic regions is as follows: VA (red), VP (green), DA  
 178 (blue), and DP (yellow) thalamus. VA: ventral anterior thalamus; VP: ventral posterior thalamus; DA:  
 179 dorsal anterior thalamus; DP: dorsal posterior thalamus. Source data are provided as a Source Data file.

180

## 181 Region-specific effects of LIFU on visual perception

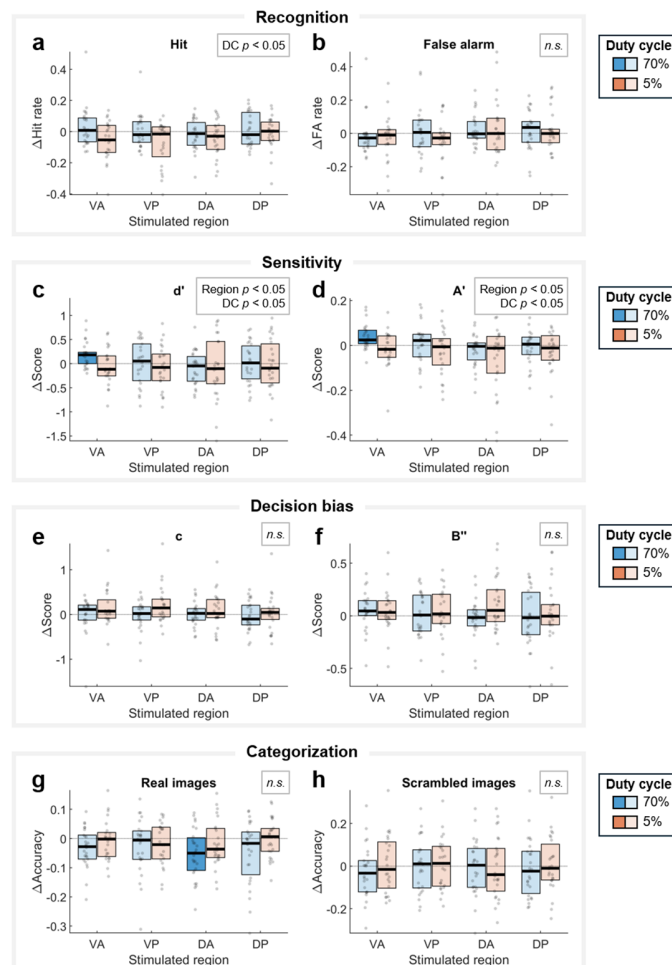
182 To mitigate individual variability, we calculated the changes of each perceptual outcome relative  
 183 to the baselines (see also the results without baseline subtraction in [Supplementary Fig. 5](#)). We

184 performed a linear mixed-effects model ANOVA to assess both main and interaction effects  
185 specific to stimulated region and duty cycle (see **Source Data** for full statistics). We also conducted  
186 additional statistical tests comparing each condition against its corresponding baseline in a  
187 region-specific manner.

188 Sensitivity metrics (parametric:  $d'$  and non-parametric:  $A'$ ) demonstrated region-specific effects,  
189 particularly for the 70% duty cycle (**Fig. 3c,d**). The ANOVA revealed significant main effects for  
190 both stimulated region ( $d'$ :  $p = 0.0438$ ;  $A'$ :  $p = 0.0393$ ) and duty cycle ( $d'$ :  $p = 0.0463$ ;  $A'$ :  $p =$   
191  $0.0362$ ). A 70% duty cycle sonication applied to the VA thalamus resulted in a significant increase  
192 in sensitivity compared to the baseline ( $d'$ :  $p = 0.0096$ ;  $A'$ :  $p = 0.0105$ ). Additionally, we observed  
193 that sensitivity increase was higher when the lateral deviation of LIFU was smaller  
194 (**Supplementary Fig. 6**), further supporting the region-specificity of this effect.

195 The hit rate exhibited a significant main effect of duty cycle ( $p = 0.0055$ ; **Fig. 3a**), where 70% duty  
196 cycle showed higher hit rate than 5% duty cycle. Regarding categorization accuracy, a significant  
197 decrease was observed specifically for real images under the 70% duty cycle when targeting the  
198 DA thalamus ( $p = 0.0002$ ; **Fig. 3g**). No changes were detected in the false alarm rate, decision  
199 bias, or the accuracy for scrambled images ( $p > 0.05$ ; **Fig. 3b,e,f,h**).

200



201

202 **Fig. 3: Region-specific changes in recognition performance under LIFU.** Changes in perceptual  
203 outcomes including **a** hit rate, **b** false alarm rate, **c** parametric sensitivity metric  $d'$ , **d** non-parametric  
204 sensitivity metric  $A'$ , **e** parametric decision bias metric  $c$ , **f** non-parametric decision bias metric  $B''$ , **g**  
205 categorization accuracy for real images, and **h** categorization accuracy for scrambled images. All values  
206 are baseline-subtracted. Darker solid boxes denote significant region-specific deviations from zero (FDR-  
207 corrected,  $p < 0.05$ , Wilcoxon signed-rank test, two-sided). ANOVA results are displayed in top-left of each  
208 subplot. The *n.s.* indicates non-significance. Box plots show the median, upper, and lower quartiles (VA 70%  
209 DC:  $n = 26$ ; VA 5% DC:  $n = 25$ ; VP 70% DC:  $n = 26$ ; VP 5% DC:  $n = 25$ ; DA 70% DC:  $n = 27$ ; DA 5% DC:  
210  $n = 26$ ; DP 70% DC:  $n = 27$ ; DP 5% DC:  $n = 27$ ). FA: false alarm; DC: duty cycle; VA: ventral anterior  
211 thalamus; VP: ventral posterior thalamus; DA: dorsal anterior thalamus; DP: dorsal posterior thalamus.  
212 Statistics and source data are provided as a Source Data file.

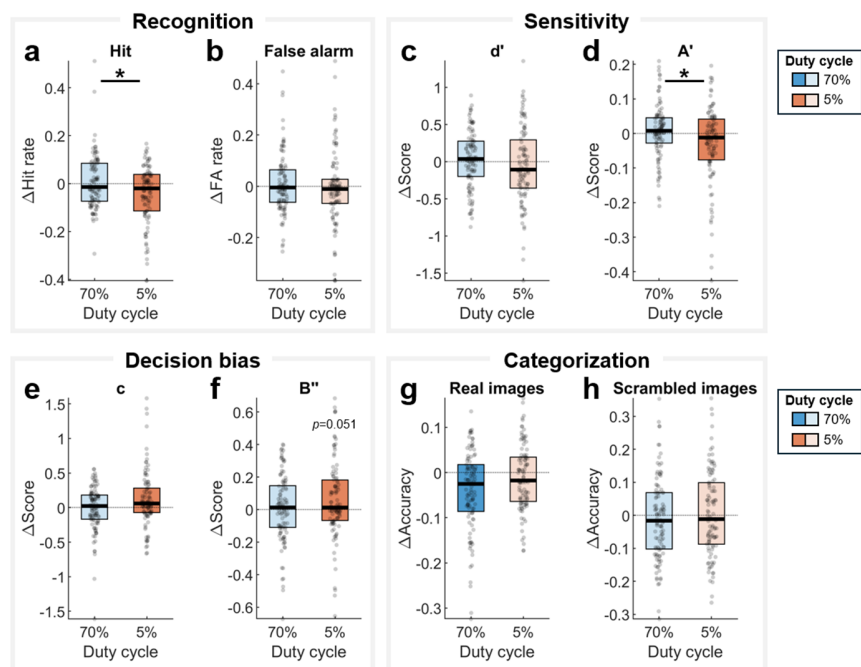
213

### 214 **Region-independent effects of LIFU on visual perception**

215 We further investigated potential effects common to all thalamic regions, which could be masked  
216 when analyzing individual thalamic regions due to inter-subject or inter-regional variability. We  
217 thus aggregated the perceptual outcomes during the four LIFU-ON blocks (see the results without  
218 baseline subtraction in [Supplementary Fig. 7](#); see [Source Data](#) for full statistics). We found that  
219 the hit rate exhibited a significant difference between the two duty cycles ( $p = 0.0026$ , Mann-  
220 Whitney U test, two-sided; [Fig. 4a](#)). Specifically, the 5% duty cycle resulted in a significant  
221 decrease in the hit rate below baseline ( $p = 0.0042$ , Wilcoxon signed-rank test, two-sided).  
222 Consistent with the decrease in hit rate, we observed an increase in decision bias metrics with 5%  
223 duty cycle sonication ( $c$ :  $p = 0.0109$ ;  $B''$ :  $p = 0.0510$ ; Wilcoxon signed-rank test, two-sided),  
224 indicating a more conservative approach in object recognition ([Fig. 4e,f](#)).

225 Regarding sensitivity, no significant change was observed relative to the baseline ([Fig. 4c,d](#)),  
226 although  $A'$  exhibited a difference between the two duty cycles ( $p = 0.0224$ , Mann-Whitney U test,  
227 two-sided), with a slight increase at 70% and a decrease at 5%. Categorization accuracy for real  
228 images significantly decreased under the 70% duty cycle ( $p = 0.0002$ , Wilcoxon signed-rank test,  
229 two-sided; [Fig. 4g](#)). No significant changes were detected for false alarm rate and accuracy for  
230 scrambled images ([Fig. 4b,h](#)).

231



232

233 **Fig. 4: Region-independent changes in visual perception under LIFU.** Changes in perceptual outcomes  
234 including **a** hit rate, **b** false alarm rate, **c** parametric sensitivity metric  $d'$ , **d** non-parametric sensitivity metric  
235  $A'$ , **e** parametric decision bias metric  $c$ , **f** non-parametric decision bias metric  $B''$ , **g** categorization accuracy  
236 for real images, **h** categorization accuracy for scrambled images. All values are baseline-subtracted.  
237 Results of four stimulated regions are aggregated. Darker solid boxes denote significant deviations from  
238 baseline zero (FDR-corrected,  $p < 0.05$ , Wilcoxon signed-rank test, two-sided). Asterisks indicate significant  
239 differences between two duty cycles ( $p < 0.05$ , Mann-Whitney U test, two-sided). Box plots show the median,  
240 upper, and lower quartiles (70% duty cycle:  $n = 106$ ; 5% duty cycle:  $n = 103$ ). FA: false alarm. Statistics  
241 and source data are provided as a Source Data file.

242

## 243 Functional connectivity of thalamic regions

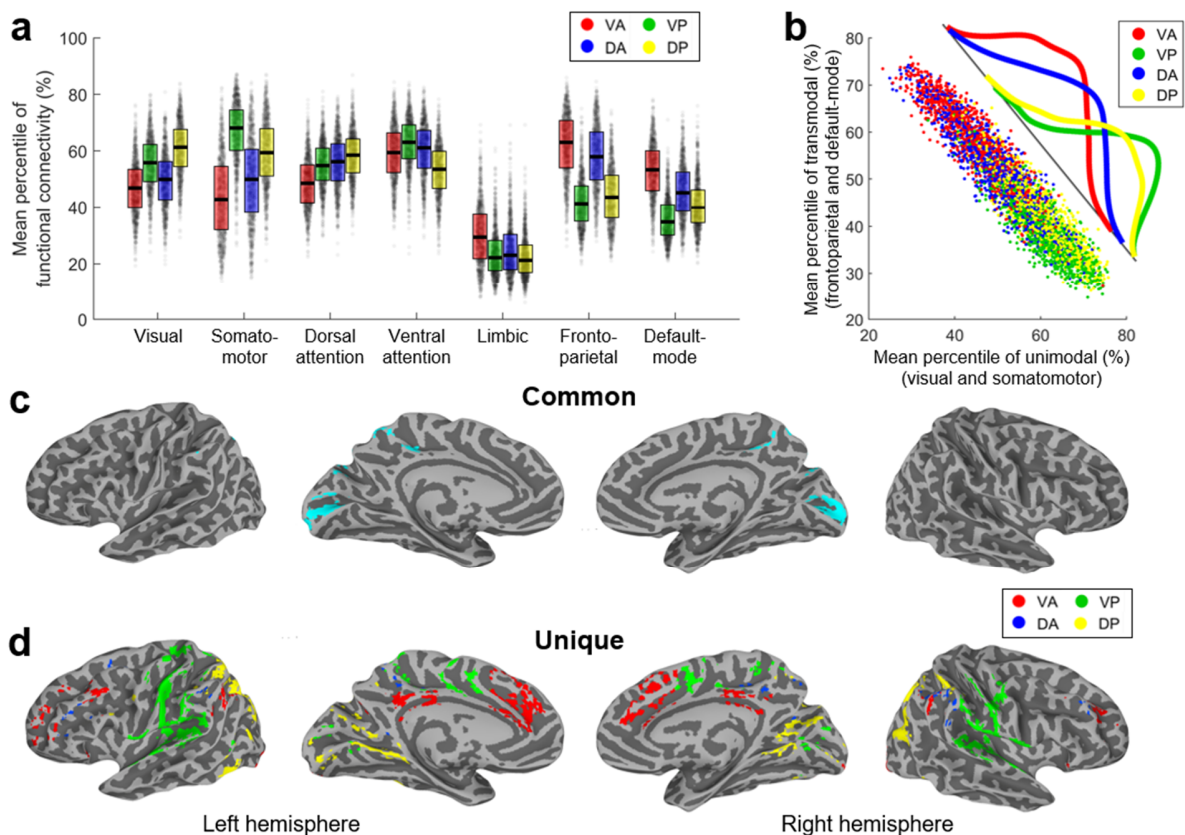
244 To gain deeper insights into the potential large-scale neural correlates of both region-independent  
245 and region-dependent effects of LIFU on visual perception, we conducted a separate analysis to  
246 investigate the connectivity profiles of the four thalamic regions, utilizing the Human Connectome  
247 Project dataset ( $n = 1009$ )<sup>56</sup>.

248 First, we assessed the connectivity profiles of these thalamic regions at the network level (Fig.  
249 5a,b). In line with our prior research<sup>29</sup>, we observed a graded shift in connectivity profiles along a  
250 unimodal-transmodal gradient. The VA thalamus displayed transmodal dominance, exhibiting  
251 higher connectivity with frontoparietal and default-mode networks compared to the other three  
252 regions (red curve in Fig. 5b). This was followed by DA thalamus, with a trend towards unimodal  
253 dominance observed in DP and VP thalamus.

254 Second, we examined the thalamocortical connectivity at a finer spatial scale, specifically at the  
255 voxel level. We retained the cortical voxels exhibiting the top 10% strongest connectivity with each  
256 respective thalamic region. The connectivity profiles of the four regions showed considerable  
257 overlap, particularly within the early visual cortex (cyan regions in Fig. 5c). However, region-  
258 specific connectivity patterns were also observed. The VA thalamus was predominantly

259 connected with the medial prefrontal cortex (mPFC) and dorsolateral prefrontal cortex (red  
260 regions in Fig. 5d). The VP thalamus exhibited unique connectivity with the somatomotor and  
261 auditory cortices (green in Fig. 5d, see also Fig. 5a). The DP thalamus showed unique clusters  
262 within various regions in the visual cortex (yellow in Fig. 5d). The connectivity profile of the DA  
263 thalamus largely overlapped with the VA thalamus (Supplementary Fig. 8), with only a few unique  
264 clusters located in regions such as left dorsolateral prefrontal cortex and right temporal-parietal  
265 junction (blue in Fig. 5d).

266



267

268 **Fig. 5: Functional connectivity profiles of four thalamic regions with the cortex.** a, b Network-level  
269 analysis. a Percentile of functional connectivity strength, averaged within each cortical network obtained  
270 from the Human Connectome Project dataset. Each dot represents an individual. Box plots show the  
271 median, upper, and lower quartiles ( $n = 1009$ ). b Distribution of mean percentiles of functional connectivity  
272 strength for unimodal (visual and somatomotor) and transmodal (frontoparietal and default-mode)  
273 networks for each thalamic region ( $n = 1009$ ). Curves represent kernel-smoothed histograms across the direction of  
274 maximal variance. c, d Voxel-based analysis. Cortical regions with the top 10% strongest connectivity with  
275 the thalamus, c common across all four thalamic regions and d unique to each thalamic region. VA: ventral  
276 anterior thalamus; VP: ventral posterior thalamus; DA: dorsal anterior thalamus; DP: dorsal posterior  
277 thalamus. Source data are provided as a Source Data file.

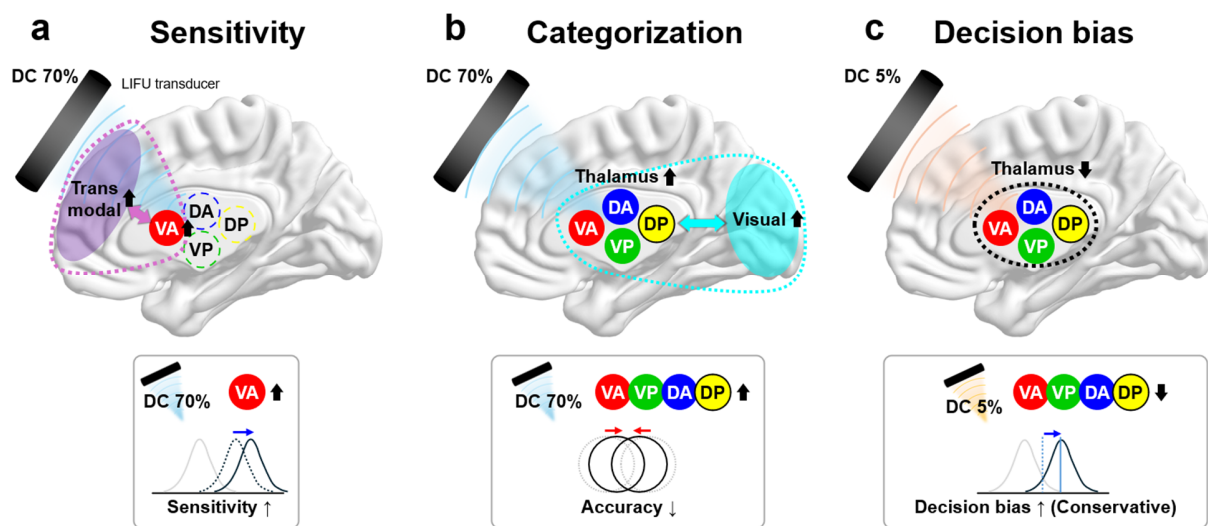
278

279

280 **DISCUSSION**

281 This study aimed to illuminate how different thalamic nuclei modulate conscious perception.  
282 Through targeted LIFU neuromodulation, we uncovered a unique role for the transmodal-  
283 dominant ventral anterior (VA) thalamus in modulating the sensitivity of conscious perception.  
284 Moreover, we observed both common (region-independent) and duty cycle dependent effects of  
285 LIFU on decision bias and categorization accuracy in object recognition, as summarized in Fig. 6.  
286 Notably, the VA thalamus, which played the most prominent role in conscious perception, was  
287 more closely functionally connected with medial and dorsolateral prefrontal cortex. Collectively,  
288 our research provides a valuable causal insight into the unimodal-transmodal functional  
289 organization of the thalamus.

290



291

292 **Fig. 6: Summary of LIFU effects on visual perception.** **a** Sensitivity increases when the VA thalamus is  
293 stimulated at the 70% duty cycle. This is associated with increased functional connectivity between the VA  
294 thalamus and transmodal areas compared with other thalamic nuclei. **b** Decrease in categorization  
295 accuracy is observed nonspecifically across all thalamic regions at the 70% duty cycle, potentially driven  
296 by interactions between the thalamus and the visual network (cyan). **c** Decision bias increases (recognition  
297 being more conservative) by the 5% duty cycle in region-independent manner. VA: ventral anterior thalamus;  
298 VP: ventral posterior thalamus; DA: dorsal anterior thalamus; DP: dorsal posterior thalamus.

299

300 Our key finding is the unique role of the transmodal-dominant VA thalamus in conscious  
301 perception (Fig. 6a). Being nonspecific and matrix-rich, VA thalamus likely interacts extensively  
302 with thick-tufted layer-5 pyramidal neurons in the cortex, promoting large-scale cortical integration  
303 essential for conscious sensory processing<sup>1,17,31,33,57</sup>. This also support theoretical frameworks  
304 such as thalamic gating mechanisms and dendritic integration theory, suggesting that matrix cells  
305 in the higher-order thalamus may modulate the threshold for conscious perception by influencing  
306 the bursting activity of thick-tufted layer-5 pyramidal neurons in the cortex<sup>1,17,25,58</sup>. These matrix  
307 cells, with their diffuse connectivity, are known to facilitate the entry of sensory content into  
308 consciousness, potentially by lowering the activation threshold of layer-5 pyramidal neurons<sup>17,36</sup>.  
309 By activating the VA thalamus, our LIFU intervention likely increases dendritic integration in layer-

310 5 pyramidal neurons, promoting widespread cortical bursting, thereby increasing perceptual  
311 sensitivity (further discussion on duty cycle-dependence follows below).

312 Furthermore, the VA thalamus encompasses the intralaminar nuclei, with projections innervating  
313 various cortical and subcortical regions<sup>18,23,59</sup>. Electrical stimulation of these nuclei via implanted  
314 electrodes has been shown to awaken non-human primates from anesthesia<sup>22,32,37</sup> and aid in the  
315 recovery of consciousness in patients with neuropathological conditions<sup>60–62</sup>. Similarly,  
316 microinjection of nicotine or potassium channel-blocking antibodies into these nuclei has restored  
317 consciousness in rodents<sup>63,64</sup>. Moreover, previous LIFU study targeting these nuclei demonstrated  
318 improvements in patients with disorders of consciousness<sup>65</sup>. Our findings provide preliminary  
319 evidence that the intralaminar nuclei might influence the qualitative aspect of conscious  
320 perception, in addition to modulating the state of consciousness.

321 One important question is whether the increased sensitivity of conscious perception was due to  
322 the VA thalamus being excited. In contrast to prior human LIFU studies that employed only one  
323 duty cycle<sup>55,66–68</sup>, we incorporated two duty cycles (70% vs. 5%) into our experimental design.  
324 LIFU is thought to selectively activate excitatory vs. inhibitory neurons depending on the duty  
325 cycle<sup>48,69</sup>. Thus, prior studies suggested that LIFU exerts a general excitatory effect at high duty  
326 cycles (e.g., > 50%) and an inhibitory effect at low duty cycles (e.g., < 20%)<sup>49,69–72</sup>. Based on this,  
327 we suggest that 70% duty cycle LIFU on the VA thalamus has induced an excitatory effect. This  
328 interpretation is also supported by previous studies. For example, Wu et al. demonstrated that  
329 higher pre-stimulus activity in the VA thalamus predicts greater sensitivity in conscious  
330 perception<sup>12</sup>. Therefore, exciting the VA thalamus may elevate its overall activity level, leading to  
331 heightened perceptual sensitivity. Furthermore, given the strong bidirectional excitatory  
332 connections<sup>73</sup> and functional connectivity (Fig. 5d) between the VA thalamus and transmodal  
333 areas such as the mPFC, VA thalamus stimulation with a 70% duty cycle may indirectly excite  
334 the mPFC. This is also supported by evidence that single-pulse electrical stimulation of the VA  
335 activates the mPFC<sup>74</sup>. Higher pre-stimulus mPFC activity also predicts greater perceptual  
336 sensitivity—a prediction intriguingly aligned with the previous findings<sup>12</sup>. Collectively, these  
337 observations suggest that LIFU with a 70% duty cycle induced an excitatory effect on the VA  
338 thalamus, which in turn, co-activated the mPFC. This dual activation could underlie the observed  
339 increase in perceptual sensitivity.

340 Regarding the region-independent decrease in categorization accuracy for real images observed  
341 with 70% duty cycle (Fig. 6b), we speculate that this effect might stem from the common functional  
342 connectivity of the thalamic regions with the visual cortex (Fig. 5c). Assuming that exciting these  
343 thalamic areas may lead to co-activation of the visual cortex, this observation aligns with previous  
344 work demonstrating a negative correlation between the pre-stimulus activity of the visual network  
345 and categorization accuracy<sup>12</sup>.

346 Regarding LIFU at 5% duty cycle, we observed common (region-independent) effects that led to  
347 more conservative decision bias (Fig. 6c). We hypothesize that this duty cycle likely induced an  
348 inhibitory neural effect, aligning with a previously-reported negative correlation between pre-  
349 stimulus thalamic activity and decision bias<sup>12</sup>. Further supporting our interpretation, prior research  
350 showed that applying LIFU at 5% duty cycle to the thalamus produced anti-nociceptive effects,  
351 suggesting a potential inhibitory influence on sensory processing<sup>55</sup>.

352 Methodologically, our work represents a significant advancement in human LIFU studies. While  
353 regional targeting within the subcortex has been previously demonstrated in rodents<sup>49</sup>, our work

354 presents the first known instance of multiple regional-level stimulations within the human thalamus.  
355 We achieved targeting of each thalamic region with sub-centimeter precision, confirmed by post-  
356 hoc analysis showing minimal overlap in the distributions of the beam centers (Fig. 2g,h). Thinking  
357 of future clinical applications, we also eliminated the reliance on brain imaging in individual  
358 subjects and thus expedited the experimental procedure; our strategy used an individually  
359 rescaled template image for LIFU targeting, thereby mitigating the need for anatomical imaging,  
360 e.g., computed tomography (CT) or T1 magnetic resonance imaging (MRI). Thus, our approach  
361 could enable LIFU application in populations where MRI scans are challenging, such as in infants,  
362 individuals with implanted medical devices, or those with severe claustrophobia.

363 We verified that the template rescaling method that we implemented meets the desired targeting  
364 accuracy. Our strategy achieved small deviations of  $1.7 \pm 0.6$  mm relative to the actual T1  
365 anatomical image (Supplementary Fig. 4). The validity of the template rescaling method is also  
366 supported by effect size increase as the lateral deviation of the beam center from the intended  
367 target (as determined by rescaled template image) decreased (Supplementary Fig. 6). Notably,  
368 the average lateral deviation of the beam from the target ( $2.3 \pm 1.0$  mm, Fig. 2i) was comparable  
369 to the beam radius (2.5 mm). This was also comparable to or better than those in previous works  
370 (deviation ranging from 3 to 9 mm), reinforcing the robustness and precision of our targeting  
371 approach<sup>55,75</sup>.

372 While previous research demonstrated the potential for LIFU to induce long-lasting effects ranging  
373 from hours to weeks<sup>76–78</sup>, we did not observe persistent changes as evidenced by the comparison  
374 between Baseline-1 and Baseline-2 data (Supplementary Fig. 2). This discrepancy may be  
375 attributed to two factors. First, the estimated intensity of our LIFU stimulation ( $0.09 \pm 0.07$  W cm<sup>-2</sup>)  
376 might have been insufficient to trigger long-term modifications. Second, the visual system, being  
377 highly adaptable and dynamic, might respond differently to LIFU compared to domains like  
378 addiction, anxiety, or depression where longer-term effects have been observed<sup>72,76,77</sup>. To better  
379 understand the implications of LIFU for scientific study and therapeutic application, future  
380 investigations should assess the factors that influence the duration of sonication effects.

381 Our study has limitations. First, the effect size of the LIFU-induced modulation of conscious  
382 perception was small (e.g., Cohen's  $d = 0.3$  for sensitivity increase during VA thalamus excitation).  
383 This might be due to the low intensity of LIFU, primarily caused by significant energy loss ( $\approx 90\%$ )  
384 from ultrasound attenuation through the human skull<sup>79</sup>. Further attenuation could have resulted  
385 from hair and air pockets. Advanced approaches like direct attenuation measurement and  
386 compensation may mitigate this problem<sup>79</sup>.

387 Moreover, the current FDA intensity guidelines (e.g., spatial-peak temporal-average intensity  $I_{spta}$   
388 =  $0.72$  W cm<sup>-2</sup>) are based on diagnostic and imaging ultrasound devices, and specific guidelines  
389 for LIFU on human brain are lacking<sup>80</sup>. Future studies should advocate for updated FDA guidelines  
390 specific to LIFU in the human brain, as current evidence suggests that higher intensities, tested  
391 safely in animal studies, may produce more robust effects without causing thermal damage<sup>49,81,82</sup>.

392 Second, the region-independent effects might be confounded by the potential influence of auditory  
393 artifacts<sup>83</sup>. However, the observed outcomes cannot be solely explained by auditory effects.  
394 Sonication with 5% duty cycle generated more noticeable sound due to the fixed time-averaged  
395 intensity compared to the 70% duty cycle leading to a higher percentage of participants reporting  
396 awareness of the sound at 5% (93% vs. 52% of participants, see Source Data). If auditory artifacts  
397 were the primary factor influencing the results, then we would expect the 5% duty cycle to have

398 a greater effect on perceptual outcomes, and in the same direction as the effects at the 70% duty  
399 cycle. However, we observed opposite effects between the two duty cycles on measures such as  
400 hit rate and sensitivity (Fig. 3a,c,d), as well as the effects unique to the 70% duty cycle such as  
401 the lower categorization accuracy for real images (Fig. 4g). These findings support the specificity  
402 of the observed effects. Nonetheless, to better isolate and understand the potential confounding  
403 effects of auditory artifacts, future research may include a sham control with replicated sound  
404 playback, or masking of the transducer sound during LIFU stimulation.

405 In conclusion, our findings illuminate the causal roles of distinct thalamic regions in conscious  
406 perception, particularly highlighting the unique contribution of the transmodal-dominant ventral  
407 anterior (VA) thalamus in modulating perceptual sensitivity. These results provide causal insight  
408 into the intricate unimodal-transmodal functional organization of the thalamus.

409

## 410 METHODS

411 **Participants.** The study protocol (ClinicalTrials.gov ID: NCT06083493) was approved by the  
412 Institutional Board Review of the University of Michigan Medical School. A total 60 participants  
413 (age:  $25.9 \pm 6.3$  years, mean  $\pm$  SD; 38 females, 22 males) participated in the experiment. All  
414 subjects provided written informed consent prior to the experiment and were compensated. All  
415 subjects were right-handed, did not have any hearing loss, and were not colorblind, and had  
416 normal or corrected-to-normal vision. Although hair shaving was not required for this study, seven  
417 participants chose to shave their right temple in exchange for additional compensation.  
418 Participants were assigned to one of two equal-sized groups (duty cycle = 70% and 5%) by a  
419 random number generator, each comprising 30 participants. Since the neuromodulation effect is  
420 dependent on various factors, such as parameters and target regions, determining a prior effect  
421 size is challenging. However, we planned for a subject number of  $n = 30$  per group, exceeding  
422 the mean sample size ( $n = 19$ ) reported in the literature<sup>84</sup>. One subject who performed a different  
423 visual task was not included in data analysis. Three subjects with technical issues during targeting  
424 were excluded from data analysis. One subject did not complete the task due to technical issues  
425 in perceptual threshold determination. One subject was excluded because the hit rate during  
426 Baseline-1 was too low ( $< 15\%$ ). Thus, a total sample size was  $n = 54$  (70% duty cycle:  $n = 27$ ;  
427 5% duty cycle:  $n = 27$ ; see also **Supplementary Fig. 9** for a flow chart). Sex or gender analysis  
428 was not conducted because there were no sex or gender specific hypotheses regarding the  
429 influence of ultrasound neuromodulation on visual perception. Participants were blinded to the  
430 intervention conditions by providing identical procedural setups and device operations across both  
431 groups, ensuring that all participants did not know the specific duty cycle assignment.

432 **LIFU devices and parameters.** LIFU was administered using the BrainSonix BXPulsar 1002  
433 LIFU System (BrainSonix Corporations, Sherman Oaks, CA, USA). This system includes a single  
434 transducer with a 61.5 mm diameter and 80.7 mm focal depth. The focal depth was also validated  
435 by Blatek Ultrasonic Transducers (Boalsburg, PA, USA). This transducer is mounted in a plastic  
436 housing and sealed with a thin polyethylene membrane. To identify the optimal placement for the  
437 transducer on the participant's head, we utilized the Brainsight Neuro-Navigation System (Rogue  
438 Research, Montreal, Quebec, Canada).

439 Sonication parameters are determined as follows: Fundamental frequency: 650 kHz; Pulse  
440 repetition frequency: 10 Hz; Pulse width: 5 ms; Duty cycle: 70% and 5%; Sonication duration: 30  
441 s; Inter-sonication interval: 30 s; Sonication per block: 12;  $I_{spta}$ :  $0.72 \text{ W cm}^{-2}$ . The intensity is

442 calculated using the US FDA's derating method for diagnostic ultrasound systems, which  
443 assumes a uniform tissue attenuation rate of  $0.3 \text{ dB cm}^{-1} \text{ MHz}^{-1}$ .

444 **Transducer setup.** Aquasonic Ultrasound Gel was applied to the right temple before positioning  
445 the transducer, ensuring that all hairs in the area were thoroughly coated with gel to enhance  
446 ultrasound transmission. The transducer was then positioned on the right temple and secured  
447 with two adjustable fabric bands: one band ran from the chin over the top of the head, and the  
448 other band passed from the forehead to the back of the head. Additional self-adhering bandages  
449 were used on top of the fabric bands to fine-tune the angle of the transducer for precise alignment.  
450 During the LIFU stimulation, we recorded the coordinates of the target location and the contact  
451 point between the transducer and the skin for post-hoc analysis.

452 **Target locations.** Following a previous thalamic parcellation scheme<sup>85</sup>, the thalamus was  
453 coarsely divided into four regions: ventral anterior (VA), ventral posterior (VP), dorsal anterior  
454 (DA), dorsal posterior (DP). Given the lack of evidence for functional lateralization in the thalamus,  
455 we opted to target the left hemisphere for convenience. The center coordinates for the four regions  
456 in the MNI space are as follows. Left VA: (-8 mm, -11 mm, 6 mm), Left VP: (-13 mm, -23 mm, 2  
457 mm), Left DA: (-12 mm, -23 mm, 12 mm), Left DP: (-16 mm, -31 mm, 2 mm). Notably, due to the  
458 elongated shape of the beam (Fig. 2a), it is possible that part of the right thalamus may have been  
459 partially affected.

460 **Head size measurement.** We used a digital caliper to measure head size in three dimensions:  
461 width, depth, and side-to-top distance (Fig. 1b). Head width was measured as the distance  
462 between the left and right supratragic notches, which are indentations in the ear cartilage right  
463 above the tragus. Head depth was measured from the most posterior (back) point to the most  
464 anterior (front) point of the head. The side-to-top distance was defined as the measurement from  
465 the one supratragic notch to the highest top point of the head.

466 **Template rescaling method.** We rescaled the ICBM 2009c Nonlinear Asymmetric template of  
467 the MNI152 linear template to match each participant's head size based on the three measured  
468 dimensions. The head height, defined as the height of a triangle formed by the top of the head,  
469 the supratragic notch, and the center of the head at the plane of the supratragic notch, was  
470 calculated using the formula:

$$Height = \sqrt{(Side-to-Top Distance)^2 - (Width)^2} \quad (1)$$

471 The default head size measurements of the MNI template were as follows: width: 16 cm, depth:  
472 21 cm, and height: 15 cm. We then calculated the size ratio between the MNI template and the  
473 participant's head dimensions. The NIFTI image of the MNI template was resliced using B-spline  
474 interpolation to adjust to the participant's head size.

475 We performed a separate analysis with five subjects to validate the template rescaling method.  
476 For these subjects, we obtained actual anatomical T1 images and generated rescaled template  
477 images using the described method. For both the actual T1 and rescaled template images, we  
478 identified the real-space coordinates corresponding to four left thalamic regions based on their  
479 MNI-space coordinates. After coregistering the two images, we calculated the Euclidean  
480 distances between the coordinates derived from the actual T1 images and those from the rescaled  
481 template images for each thalamic region.

482 **Ultrasound intensity and thermal simulation.** We employed SimNIBS pipeline (SimNIBS  
483 v4.1.0, <https://simnibs.github.io/simnibs/build/html/index.html>) to differentiate skin, skull, and  
484 brain within the rescaled template brain images<sup>86</sup>. We then simulated the transcranial ultrasound  
485 intensity and thermal profiles using the BabelBrain software (BabelBrain v0.3.5,  
486 <https://proteusmrighifu.github.io/BabelBrain/>)<sup>87</sup>. Within the Brainsight software (v2.5.4), we  
487 created post-hoc trajectories starting from the recorded contact points between the transducer  
488 and the skin, pointing toward the thalamus. The spatial resolution of was set to points-per-  
489 wavelength = 6 and the field was simulated 100 mm beyond the target at maximum.

490 **Experimental procedure.** The experiment was conducted in a single session lasting  
491 approximately two hours (Fig. 1a). At the beginning of the session, participants' head size was  
492 measured (details above), followed by task instructions. Participants first completed a brief  
493 practice run consisting of 30 trials (a shorter version of staircase procedure; see below). Next, the  
494 ultrasound transducer was positioned, and participants underwent the main image contrast  
495 staircase procedure involving 60 trials. Participants then engaged in the main task, which  
496 consisted of six blocks, each containing 100 trials and lasting approximately 12 minutes, for a  
497 total of 600 trials (Fig. 1a). For staircase and main task, a custom-modified version of the public  
498 code implemented for the near-threshold behavioral paradigm  
499 ([https://github.com/BiyuHeLab/NatCommun\\_Levinson2021/](https://github.com/BiyuHeLab/NatCommun_Levinson2021/)) was used with Psychophysics  
500 Toolbox executed on MATLAB R2024a<sup>8,88</sup>.

501 During the first and last blocks, LIFU was not applied (referred to as Baseline-1 and Baseline-2).  
502 During the inner four blocks, four thalamic areas are stimulated in a pre-assigned, pseudo-  
503 randomized order (determined by a random number generator), counter-balanced across the  
504 participants, with a consistent duty cycle (either 70% or 5%) within one participant.

505 **Visual stimuli.** Visual images encompassed four categories: faces, houses, human-made  
506 objects, and animals (Fig. 1g), which were used in a previous study<sup>8</sup>. The images were sourced  
507 from publicly available labeled photographs or the Psychological Image Collection at Stirling  
508 (PICS). Each category included five distinct images, resulting in a total of 20 unique real images.  
509 All images were converted to grayscale and resized to 300 × 300 pixels. The pixel intensities were  
510 normalized by subtracting the mean and dividing by the standard deviation. Subsequently, the  
511 images were processed with a 2D Gaussian smoothing filter ('imgaussfilt' function in MATLAB  
512 R2024a), using a standard deviation of 1.5 pixels and a 7 × 7 pixel kernel. Scrambled images that  
513 maintain low-level features were generated for each category by randomizing the phase of the  
514 2D Fourier transform for one image from each category.

515 The contrast of an image was defined as:

$$\text{contrast} = \frac{I_{max} - I_{min}}{2b} \quad (2)$$

516 where  $I_{max}$  and  $I_{min}$  are the intensity values of lightest and darkest pixels in the image, respectively  
517 (in the range of 0 to 255). To ensure a smooth transition to the background (set as gray, intensity  
518 = 127), the edges of all images were gradually blended by applying a Gaussian window with a  
519 standard deviation of 0.2 to the image intensity.

520 The stimuli were displayed on a 14-inch laptop (HP ProBook 440 G4) with a 60-Hz refresh rate  
521 LCD screen, set to the maximum screen brightness. The viewing distance between the screen  
522 and the participants' eyes was maintained at 65.8 ± 5.7 cm (mean ± SD). During the experiment,  
523 participants were asked to maintain constant eye-monitor distance. We also validated the

524 distance during rest periods and readjusted the position of the laptop if necessary. We did not  
525 adopt masking because masking is known to influence the visual information processing<sup>89,90</sup>.

526 **Image contrast staircase procedure.** Before the main task, participants completed the QUEST  
527 adaptive staircase procedure<sup>8,54</sup> to determine the contrast value that would yield a 50%  
528 recognition rate (i.e., the rate of “YES” response to Question-2). The QUEST procedure was  
529 similar to the main task but with shorter timing parameters. The inter-trial interval was 0.75  
530 seconds, and the delay period between the stimulus and the first question was 2 seconds. The  
531 threshold contrast was identified through a QUEST process consisting of 60 trials. Each trial was  
532 randomly assigned to one of three sets, and the staircase procedure was conducted separately  
533 for each set. Task performance was deemed acceptable if the three sets successfully converged  
534 on a specific contrast value. The staircase procedure was repeated until the convergence of the  
535 three curves was confirmed. Rather than adjusting the contrast of each image individually, the  
536 staircasing aimed for 50% recognition across all images.

537 **Main task.** Each block of the main task featured four trials per real image (80 real trials in total)  
538 and five trials per scrambled image (20 scrambled trials in total). Participants were unaware of  
539 the fact that scrambled images would appear. Participants were allowed to rest for at least 3  
540 minutes between blocks, during which the transducer was readjusted. The entire main task took  
541 about 1.5 hours to complete.

542 Each trial began with a fixation cross displayed on a gray background for a randomly determined  
543 duration between 3 and 6 seconds, following an exponential distribution to prevent participants  
544 from predicting stimulus onset (Fig. 1e). The stimulus image was then shown behind the fixation  
545 cross for 8 frames (67 ms), with the image intensity linearly increasing across frames. After the  
546 stimulus disappeared, the fixation cross remained on the screen for an additional 2 seconds. Each  
547 trial concluded with two sequential questions about the stimulus, each displayed for up to 3  
548 seconds.

549 Question-1 asked participants to categorize the image as a face, house, object, or animal.  
550 Participants were instructed to guess the category even if they did not consciously recognize the  
551 object (four-alternative forced-choice). Question-2 assessed their subjective experience, asking  
552 whether they had a “meaningful visual experience” of the object stimulus (“YES” or “NO”). Before  
553 the practice run, participants were told that a “meaningful” stimulus was defined as something  
554 that makes sense in the real world, as opposed to random noise or meaningless shapes. They  
555 were instructed to respond “YES” even if they recognized only part of an object. Participants  
556 provided their answers by pressing buttons on a 4-key external USB keyboard placed on their lap.  
557 If participants did not respond to Question-1, it was recorded as incorrect, and for Question-2, a  
558 lack of response was recorded as “NO.”

559 **Signal detection theory analysis.** We employed signal detection theory (SDT) to examine the  
560 perceptual outcomes, focusing on sensitivity and decision bias<sup>91–93</sup>. Sensitivity measures the  
561 ability to distinguish between real images and scrambled images. We calculated both parametric  
562 and non-parametric sensitivity metrics through standard SDT analysis:  $d'$  and  $A'$ , defined as  
563 follows:

$$d' = \Phi^{-1}(H) - \Phi^{-1}(FA) \quad (3)$$

$$A' = 0.5 + \left[ \text{sign}(H - FA) \frac{(H - FA)^2 + |H - FA|}{4 \max(H, FA) - 4 H \cdot FA} \right] \quad (4)$$

564

565 where  $\Phi^{-1}$  is the inverse normal cumulative distribution function,  $H$  is the hit rate, and  $FA$  is the  
566 false alarm rate, respectively. High  $d'$  and  $A'$  values indicate better discrimination between real  
567 and scrambled images.

568 Decision bias refers to the inclination to certain response, regardless of whether the stimulus is  
569 real or scrambled. We assessed decision bias using parametric and non-parametric metrics:  $c$   
570 and  $B''$ , defined below.

$$c = -\frac{\Phi^{-1}(H) + \Phi^{-1}(FA)}{2} \quad (5)$$

$$B'' = \text{sign}(H - FA) \frac{H(1 - H) - FA(1 - FA)}{H(1 - H) + FA(1 - FA)} \quad (6)$$

571 High  $c$  and  $B''$  values indicate the tendency to say “NO” to Question-2, indicating a more  
572 conservative object recognition.

573 Following Macmillan and Kaplan’s correction, we substituted the values of false alarm or hit rate  
574 to  $1 - \frac{1}{2N_{real}}$  and  $\frac{1}{2N_{scram}}$  when  $FA = 0$  or  $H = 1$ , where  $N_{real}$  and  $N_{scram}$  refers to the number of trials  
575 showing real and scrambled images, respectively<sup>12,94</sup>.

576 **Human Connectome Project Dataset.** The dataset was obtained from the S1200 Release of the  
577 WU-Minn Human Connectome Project (HCP) database, which has been extensively described in  
578 prior studies<sup>56</sup>. The participants were healthy young adults aged 22 to 37 years. Participants who  
579 had completed two sessions of resting-state fMRI scans (Rest1 and Rest2) were included in our  
580 analysis, resulting in  $n = 1009$ . The data were collected using a customized Siemens 3T MR  
581 scanner (Skyra system) with multiband EPI. Each scanning session comprised two sequences  
582 with opposite phase encoding directions (left-to-right and right-to-left), each lasting 14 minutes  
583 and 33 seconds. The sequences were acquired with a repetition time (TR) of 720 ms, an echo  
584 time (TE) of 33.1 ms, and a voxel size of 2 mm isotropic. To maximize data quality and minimize  
585 bias from phase encoding direction, the sequences from each session were combined, resulting  
586 in a total of 29 minutes and 6 seconds. The denoised volumetric data, preprocessed through ICA-  
587 FIX, were accessed from the online HCP database. Further details on the resting-state fMRI data  
588 collection and preprocessing are available in previous publications<sup>95,96</sup>. We employed the AFNI  
589 software suite (linux\_ubuntu\_16\_64; <http://afni.nimh.nih.gov/>) for further preprocessing,  
590 encompassing resampling to a  $3 \times 3 \times 3$  mm resolution, band-pass filtering within the 0.01-0.1 Hz  
591 frequency range, spatial smoothing with a 6-mm Full Width at Half Maximum isotropic Gaussian  
592 kernel, and temporal normalization to attain zero mean and unit variance.

593 **Network-level analysis.** We parcellated the cortex into 400 regions of interest (ROIs), each  
594 assigned to one of seven canonical networks: visual, somatomotor, dorsal attention, ventral  
595 attention, limbic, frontoparietal, and default-mode networks, based on a well-established  
596 parcellation scheme<sup>97,98</sup>. Based on the Subcortical Atlas<sup>85</sup>, we extracted time courses of BOLD  
597 signal within the left VA, VP, DA, and DP thalamus. For each region, we calculated the functional  
598 connectivity across all 400 cortical ROIs. We then obtained the rank of the functional connectivity  
599 for each resting-state session (Rest1 and Rest2) and averaged these ranks across the seven  
600 networks and two sessions to calculate network-level connectivity. Lastly, we computed the

601 average rank for unimodal (visual and somatomotor) and transmodal (frontoparietal and default-  
602 mode) networks and plotted them in a 2D space.

603 **Voxel-based analysis.** Mean time courses were extracted from left VA, VP, DA, and DP  
604 thalamus, serving as seed regions for functional connectivity analysis. Seed-based maps  
605 (Pearson correlation, Fisher-z transformed) were generated for each participant and region.  
606 Group-level z-score maps were generated by standardizing individual connectivity values  
607 (subtracting the mean and dividing by the standard deviation across participants). Within the  
608 cortex, we retained the top 10% of voxels with the highest connectivity. This analysis was  
609 performed independently for Rest1 and Rest2 sessions, and their overlap was used to ensure  
610 consistency. Unique and common clusters of high-connectivity voxels were then identified for  
611 each thalamic region.

612 **Statistics.** To ensure stabilization of task performance, the first ten trials of each block were  
613 omitted from the analysis. Due to technical issues, a few participants failed to complete specific  
614 LIFU-ON blocks, which were consequently excluded from the analysis (Fig. 3, 4). The affected  
615 blocks and the number of participants were as follows: VA 70% DC ( $n = 1$ ), VA 5% DC ( $n = 2$ ),  
616 VP 70% DC ( $n = 1$ ), VP 5% DC ( $n = 2$ ), and DA 5% DC ( $n = 1$ ). Additionally, for one subject in the  
617 5% DC group, the lateral deviation value was not recorded for VP (Fig. 2i). Beam center locations  
618 were not recorded for a few participants, resulting in their omission from the beam deviation  
619 analysis (Fig. 2j). The numbers of participants with missing beam center location data were: VA  
620 ( $n = 4$ ); VP ( $n = 6$ ); DA ( $n = 3$ ); DP ( $n = 3$ ). Furthermore, the locations of the transducer on the  
621 scalp were not recorded for a few participants, leading to their exclusion from the intensity  
622 estimation analysis (Fig. 2k). The numbers of participants with missing transducer location data  
623 were: VA ( $n = 9$ ); VP ( $n = 10$ ); DA ( $n = 9$ ); DP ( $n = 9$ ).

624 In Fig. 3, baseline-subtracted perceptual outcomes were evaluated by two statistical tests. First,  
625 we assessed the main and interaction effects of duty cycle and stimulation region using a linear  
626 mixed-effects model ANOVA. Additionally, we tested whether the distribution of perceptual  
627 outcomes for each duty cycle and stimulation region deviated from zero using the Wilcoxon  
628 signed-rank test (two-sided). Eight tests (four regions  $\times$  two duty cycles) were corrected for  
629 multiple comparisons using false discovery rate (FDR) method. In Fig. 4, baseline-subtracted  
630 perceptual outcomes were aggregated across stimulation regions and compared between the two  
631 duty cycles using the Mann-Whitney U test (two-sided). Similar to the analysis in Fig. 3, we also  
632 tested whether the distributions deviated from zero using the Wilcoxon signed-rank test (two-  
633 sided). Full statistics of main and supplementary analyses are included in [Source Data](#).

634

#### 635 **DATA AVAILABILITY**

636 Source data are provided with this paper. The HCP dataset is available from online repository  
637 (<https://www.humanconnectome.org/>).

638

#### 639 **CODE AVAILABILITY**

640 Code for near-threshold paradigm is available at Github  
641 ([https://github.com/BiyuHeLab/NatCommun\\_Levinson2021/](https://github.com/BiyuHeLab/NatCommun_Levinson2021/))<sup>8</sup>. Custom-built code for template  
642 rescaling will become available at Github.

643

644 **REFERENCES**

- 645 1. Aru, J., Suzuki, M. & Larkum, M. E. Cellular Mechanisms of Conscious Processing. *Trends in*  
646 *Cognitive Sciences* **24**, 814–825 (2020).
- 647 2. Dehaene, S., Changeux, J.-P., Naccache, L., Sackur, J. & Sergent, C. Conscious, preconscious,  
648 and subliminal processing: a testable taxonomy. *Trends Cogn Sci* **10**, 204–211 (2006).
- 649 3. Dehaene, S. & Changeux, J.-P. Experimental and Theoretical Approaches to Conscious  
650 Processing. *Neuron* **70**, 200–227 (2011).
- 651 4. Koch, C., Massimini, M., Boly, M. & Tononi, G. Neural correlates of consciousness: progress  
652 and problems. *Nat Rev Neurosci* **17**, 307–321 (2016).
- 653 5. Mashour, G. A. & Hudetz, A. G. Neural Correlates of Unconsciousness in Large-Scale Brain  
654 Networks. *Trends in Neurosciences* **41**, 150–160 (2018).
- 655 6. Seth, A. K. & Bayne, T. Theories of consciousness. *Nat Rev Neurosci* **23**, 439–452 (2022).
- 656 7. Storm, J. F. *et al.* An integrative, multiscale view on neural theories of consciousness. *Neuron*  
657 S0896627324000886 (2024) doi:10.1016/j.neuron.2024.02.004.
- 658 8. Levinson, M., Podvalny, E., Baete, S. H. & He, B. J. Cortical and subcortical signatures of  
659 conscious object recognition. *Nat Commun* **12**, 2930 (2021).
- 660 9. Podvalny, E., Flounders, M. W., King, L. E., Holroyd, T. & He, B. J. A dual role of prestimulus  
661 spontaneous neural activity in visual object recognition. *Nat Commun* **10**, 3910 (2019).
- 662 10. Takahashi, N., Oertner, T. G., Hegemann, P. & Larkum, M. E. Active cortical dendrites modulate  
663 perception. *Science* **354**, 1587–1590 (2016).
- 664 11. Van Vugt, B. *et al.* The threshold for conscious report: Signal loss and response bias in visual  
665 and frontal cortex. *Science* **360**, 537–542 (2018).
- 666 12. Wu, Y., Podvalny, E., Levinson, M. & He, B. J. Network mechanisms of ongoing brain activity's  
667 influence on conscious visual perception. *Nat Commun* **15**, 5720 (2024).
- 668 13. Martín-Signes, M., Chica, A. B., Bartolomeo, P. & Thiebaut de Schotten, M. Streams of  
669 conscious visual experience. *Commun Biol* **7**, 908 (2024).

- 670 14. Bell, P. T. & Shine, J. M. Subcortical contributions to large-scale network communication.  
671 *Neuroscience & Biobehavioral Reviews* **71**, 313–322 (2016).
- 672 15. Shine, J. M. *et al.* Human cognition involves the dynamic integration of neural activity and  
673 neuromodulatory systems. *Nat Neurosci* **22**, 289–296 (2019).
- 674 16. Shine, J. M., Lewis, L. D., Garrett, D. D. & Hwang, K. The impact of the human thalamus on  
675 brain-wide information processing. *Nat Rev Neurosci* **24**, 416–430 (2023).
- 676 17. Whyte, C. J., Redinbaugh, M. J., Shine, J. M. & Saalman, Y. B. Thalamic contributions to the  
677 state and contents of consciousness. *Neuron* **112**, 1611–1625 (2024).
- 678 18. Jones, E. G. The thalamic matrix and thalamocortical synchrony. *Trends in Neurosciences* **24**,  
679 595–601 (2001).
- 680 19. Jones, E. G. Synchrony in the Interconnected Circuitry of the Thalamus and Cerebral Cortex.  
681 *Annals of the New York Academy of Sciences* **1157**, 10–23 (2009).
- 682 20. Usrey, W. M. & Alitto, H. J. Visual Functions of the Thalamus. *Annual Review of Vision Science*  
683 **1**, 351–371 (2015).
- 684 21. Müller, E. J. *et al.* The non-specific matrix thalamus facilitates the cortical information processing  
685 modes relevant for conscious awareness. *Cell Reports* **42**, 112844 (2023).
- 686 22. Redinbaugh, M. J. *et al.* Thalamus Modulates Consciousness via Layer-Specific Control of  
687 Cortex. *Neuron* **106**, 66-75.e12 (2020).
- 688 23. Vertes, R. P., Linley, S. B. & Rojas, A. K. P. Structural and functional organization of the midline  
689 and intralaminar nuclei of the thalamus. *Front. Behav. Neurosci.* **16**, 964644 (2022).
- 690 24. Roy, D. S., Zhang, Y., Halassa, M. M. & Feng, G. Thalamic subnetworks as units of function. *Nat*  
691 *Neurosci* **25**, 140–153 (2022).
- 692 25. Shine, J. M. The thalamus integrates the macrosystems of the brain to facilitate complex,  
693 adaptive brain network dynamics. *Progress in Neurobiology* **199**, 101951 (2021).
- 694 26. Huntenburg, J. M., Bazin, P.-L. & Margulies, D. S. Large-Scale Gradients in Human Cortical  
695 Organization. *Trends in Cognitive Sciences* **22**, 21–31 (2018).

- 696 27. Margulies, D. S. *et al.* Situating the default-mode network along a principal gradient of  
697 macroscale cortical organization. *Proceedings of the National Academy of Sciences* **113**,  
698 12574–12579 (2016).
- 699 28. Murphy, C. *et al.* Distant from input: Evidence of regions within the default mode network  
700 supporting perceptually-decoupled and conceptually-guided cognition. *NeuroImage* **171**, 393–  
701 401 (2018).
- 702 29. Huang, Z., Mashour, G. A. & Hudetz, A. G. Propofol Disrupts the Functional Core-Matrix  
703 Architecture of the Thalamus in Humans. *bioRxiv* 2024.01.23.576934 (2024)  
704 doi:10.1101/2024.01.23.576934.
- 705 30. Müller, E. J. *et al.* Core and matrix thalamic sub-populations relate to spatio-temporal cortical  
706 connectivity gradients. *NeuroImage* **222**, 117224 (2020).
- 707 31. Aru, J., Suzuki, M., Rutiku, R., Larkum, M. E. & Bachmann, T. Coupling the State and Contents  
708 of Consciousness. *Front. Syst. Neurosci.* **13**, (2019).
- 709 32. Bastos, A. M. *et al.* Neural effects of propofol-induced unconsciousness and its reversal using  
710 thalamic stimulation. *eLife* **10**, e60824 (2021).
- 711 33. Honjoh, S. *et al.* Regulation of cortical activity and arousal by the matrix cells of the ventromedial  
712 thalamic nucleus. *Nat Commun* **9**, 2100 (2018).
- 713 34. Munn, B. R. *et al.* A thalamocortical substrate for integrated information via critical synchronous  
714 bursting. *Proc. Natl. Acad. Sci. U.S.A.* **120**, e2308670120 (2023).
- 715 35. Shepherd, G. M. G. & Yamawaki, N. Untangling the cortico-thalamo-cortical loop: cellular pieces  
716 of a knotty circuit puzzle. *Nat Rev Neurosci* **22**, 389–406 (2021).
- 717 36. Takahashi, N. *et al.* Active dendritic currents gate descending cortical outputs in perception. *Nat*  
718 *Neurosci* **23**, 1277–1285 (2020).
- 719 37. Tasserie, J. *et al.* Deep brain stimulation of the thalamus restores signatures of consciousness  
720 in a nonhuman primate model. *Sci. Adv.* **8**, eabl5547 (2022).
- 721 38. Liu, X., Qiu, F., Hou, L. & Wang, X. Review of Noninvasive or Minimally Invasive Deep Brain  
722 Stimulation. *Front. Behav. Neurosci.* **15**, (2022).

- 723 39. Lozano, A. M. *et al.* Deep brain stimulation: current challenges and future directions. *Nat Rev*  
724 *Neurol* **15**, 148–160 (2019).
- 725 40. Bystritsky, A. *et al.* A review of low-intensity focused ultrasound pulsation. *Brain Stimulation* **4**,  
726 125–136 (2011).
- 727 41. Legon, W. *et al.* Transcranial focused ultrasound modulates the activity of primary  
728 somatosensory cortex in humans. *Nat Neurosci* **17**, 322–329 (2014).
- 729 42. Rabut, C. *et al.* Ultrasound Technologies for Imaging and Modulating Neural Activity. *Neuron*  
730 **108**, 93–110 (2020).
- 731 43. Tufail, Y., Yoshihiro, A., Pati, S., Li, M. M. & Tyler, W. J. Ultrasonic neuromodulation by brain  
732 stimulation with transcranial ultrasound. *Nat Protoc* **6**, 1453–1470 (2011).
- 733 44. Tyler, W. J. *et al.* Remote Excitation of Neuronal Circuits Using Low-Intensity, Low-Frequency  
734 Ultrasound. *PLoS ONE* **3**, e3511 (2008).
- 735 45. Yoo, S.-S. *et al.* Focused ultrasound modulates region-specific brain activity. *NeuroImage* **56**,  
736 1267–1275 (2011).
- 737 46. Tufail, Y. *et al.* Transcranial Pulsed Ultrasound Stimulates Intact Brain Circuits. *Neuron* **66**, 681–  
738 694 (2010).
- 739 47. Darrow, D. P., O'Brien, P., Richner, T. J., Netoff, T. I. & Ebbini, E. S. Reversible neuroinhibition  
740 by focused ultrasound is mediated by a thermal mechanism. *Brain Stimulation* **12**, 1439–1447  
741 (2019).
- 742 48. Dell'Italia, J., Sanguinetti, J. L., Monti, M. M., Bystritsky, A. & Reggente, N. Current State of  
743 Potential Mechanisms Supporting Low Intensity Focused Ultrasound for Neuromodulation.  
744 *Front. Hum. Neurosci.* **16**, 872639 (2022).
- 745 49. Murphy, K. R. *et al.* Optimized ultrasound neuromodulation for non-invasive control of behavior  
746 and physiology. *Neuron* (2024) doi:10.1016/j.neuron.2024.07.002.
- 747 50. Blackmore, J., Shrivastava, S., Sallet, J., Butler, C. R. & Cleveland, R. O. Ultrasound  
748 Neuromodulation: A Review of Results, Mechanisms and Safety. *Ultrasound in Medicine &*  
749 *Biology* **45**, 1509–1536 (2019).

- 750 51. Fomenko, A., Neudorfer, C., Dallapiazza, R. F., Kalia, S. K. & Lozano, A. M. Low-intensity  
751 ultrasound neuromodulation: An overview of mechanisms and emerging human applications.  
752 *Brain Stimulation* **11**, 1209–1217 (2018).
- 753 52. Tyler, W. J., Lani, S. W. & Hwang, G. M. Ultrasonic modulation of neural circuit activity. *Current*  
754 *Opinion in Neurobiology* **50**, 222–231 (2018).
- 755 53. Darmani, G. *et al.* Non-invasive transcranial ultrasound stimulation for neuromodulation. *Clinical*  
756 *Neurophysiology* **135**, 51–73 (2022).
- 757 54. Watson, A. B. & Pelli, D. G. Quest: A Bayesian adaptive psychometric method. *Perception &*  
758 *Psychophysics* **33**, 113–120 (1983).
- 759 55. Badran, B. W. *et al.* Sonication of the anterior thalamus with MRI-Guided transcranial focused  
760 ultrasound (tFUS) alters pain thresholds in healthy adults: A double-blind, sham-controlled  
761 study. *Brain Stimulation* **13**, 1805–1812 (2020).
- 762 56. Van Essen, D. C. *et al.* The WU-Minn Human Connectome Project: An overview. *NeuroImage*  
763 **80**, 62–79 (2013).
- 764 57. Suzuki, M. & Larkum, M. E. General Anesthesia Decouples Cortical Pyramidal Neurons. *Cell*  
765 **180**, 666–676.e13 (2020).
- 766 58. Mukherjee, A., Lam, N. H., Wimmer, R. D. & Halassa, M. M. Thalamic circuits for independent  
767 control of prefrontal signal and noise. *Nature* **600**, 100–104 (2021).
- 768 59. Smith, Y., Raju, D. V., Pare, J.-F. & Sidibe, M. The thalamostriatal system: a highly specific  
769 network of the basal ganglia circuitry. *Trends in Neurosciences* **27**, 520–527 (2004).
- 770 60. Magrassi, L. *et al.* Results of a prospective study (CATS) on the effects of thalamic stimulation in  
771 minimally conscious and vegetative state patients. (2016) doi:10.3171/2015.7.JNS15700.
- 772 61. Schiff, N. D. *et al.* Behavioural improvements with thalamic stimulation after severe traumatic  
773 brain injury. *Nature* **448**, 600–603 (2007).
- 774 62. Schiff, N. D. *et al.* Thalamic deep brain stimulation in traumatic brain injury: a phase 1,  
775 randomized feasibility study. *Nat Med* **29**, 3162–3174 (2023).

- 776 63. Alkire, M. T., McReynolds, J. R., Hahn, E. L. & Trivedi, A. N. Thalamic Microinjection of Nicotine  
777 Reverses Sevoflurane-induced Loss of Righting Reflex in the Rat. *Anesthesiology* **107**, 264–272  
778 (2007).
- 779 64. Alkire, M. T., Asher, C. D., Franciscus, A. M. & Hahn, E. L. Thalamic Microinfusion of Antibody to  
780 a Voltage-gated Potassium Channel Restores Consciousness during Anesthesia.  
781 *Anesthesiology* **110**, 766–773 (2009).
- 782 65. Monti, M. M., Schnakers, C., Korb, A. S., Bystritsky, A. & Vespa, P. M. Non-Invasive Ultrasonic  
783 Thalamic Stimulation in Disorders of Consciousness after Severe Brain Injury: A First-in-Man  
784 Report. *Brain Stimulation* **9**, 940–941 (2016).
- 785 66. Legon, W., Bansal, P., Tyshynsky, R., Ai, L. & Mueller, J. K. Transcranial focused ultrasound  
786 neuromodulation of the human primary motor cortex. *Sci Rep* **8**, 10007 (2018).
- 787 67. Xia, X. *et al.* Time course of the effects of low-intensity transcranial ultrasound on the excitability  
788 of ipsilateral and contralateral human primary motor cortex. *NeuroImage* **243**, 118557 (2021).
- 789 68. Zadeh, A. K. *et al.* The effect of transcranial ultrasound pulse repetition frequency on sustained  
790 inhibition in the human primary motor cortex: A double-blind, sham-controlled study. *Brain*  
791 *Stimulation* **17**, 476–484 (2024).
- 792 69. Yu, K., Niu, X., Krook-Magnuson, E. & He, B. Intrinsic functional neuron-type selectivity of  
793 transcranial focused ultrasound neuromodulation. *Nat Commun* **12**, 2519 (2021).
- 794 70. Fomenko, A. *et al.* Systematic examination of low-intensity ultrasound parameters on human  
795 motor cortex excitability and behavior. *eLife* **9**, e54497 (2020).
- 796 71. Murphy, K. R. *et al.* A tool for monitoring cell type-specific focused ultrasound neuromodulation  
797 and control of chronic epilepsy. *Proceedings of the National Academy of Sciences* **119**,  
798 e2206828119 (2022).
- 799 72. Fan, J. M. *et al.* Thalamic transcranial ultrasound stimulation in treatment resistant depression.  
800 *Brain Stimulation* **17**, 1001–1004 (2024).
- 801 73. Yang, C. *et al.* Medial prefrontal cortex and anteromedial thalamus interaction regulates goal-  
802 directed behavior and dopaminergic neuron activity. *Nat Commun* **13**, 1386 (2022).

- 803 74. Wu, D. *et al.* Human anterior thalamic stimulation evoked cortical potentials align with intrinsic  
804 functional connectivity. *Neuroimage* **277**, 120243 (2023).
- 805 75. Xu, L. *et al.* Characterization of the Targeting Accuracy of a Neuronavigation-Guided  
806 Transcranial FUS System In Vitro, In Vivo, and In Silico. *IEEE Transactions on Biomedical*  
807 *Engineering* **70**, 1528–1538 (2023).
- 808 76. Mahdavi, K. D. *et al.* A pilot study of low-intensity focused ultrasound for treatment-resistant  
809 generalized anxiety disorder. *Journal of Psychiatric Research* **168**, 125–132 (2023).
- 810 77. Mahoney, J. J. *et al.* Low-intensity focused ultrasound targeting the nucleus accumbens as a  
811 potential treatment for substance use disorder: safety and feasibility clinical trial. *Front.*  
812 *Psychiatry* **14**, (2023).
- 813 78. Yaakub, S. N. *et al.* Transcranial focused ultrasound-mediated neurochemical and functional  
814 connectivity changes in deep cortical regions in humans. *Nat Commun* **14**, 5318 (2023).
- 815 79. Riis, T., Feldman, D., Mickey, B. & Kubanek, J. Controlled noninvasive modulation of deep brain  
816 regions in humans. *Commun Eng* **3**, 1–12 (2024).
- 817 80. Quarato, C. M. I. *et al.* A Review on Biological Effects of Ultrasounds: Key Messages for  
818 Clinicians. *Diagnostics (Basel)* **13**, 855 (2023).
- 819 81. Folloni, D. *et al.* Manipulation of Subcortical and Deep Cortical Activity in the Primate Brain  
820 Using Transcranial Focused Ultrasound Stimulation. *Neuron* **101**, 1109-1116.e5 (2019).
- 821 82. Qin, P. P. *et al.* The effectiveness and safety of low-intensity transcranial ultrasound stimulation:  
822 A systematic review of human and animal studies. *Neuroscience & Biobehavioral Reviews* **156**,  
823 105501 (2024).
- 824 83. Sato, T., Shapiro, M. G. & Tsao, D. Y. Ultrasonic Neuromodulation Causes Widespread Cortical  
825 Activation via an Indirect Auditory Mechanism. *Neuron* **98**, 1031-1041.e5 (2018).
- 826 84. Sarica, C. *et al.* Human Studies of Transcranial Ultrasound neuromodulation: A systematic  
827 review of effectiveness and safety. *Brain Stimulation* **15**, 737–746 (2022).
- 828 85. Tian, Y., Margulies, D. S., Breakspear, M. & Zalesky, A. Topographic organization of the human  
829 subcortex unveiled with functional connectivity gradients. *Nat Neurosci* **23**, 1421–1432 (2020).

- 830 86. Thielscher, A., Antunes, A. & Saturnino, G. B. Field modeling for transcranial magnetic  
831 stimulation: A useful tool to understand the physiological effects of TMS? in *2015 37th Annual*  
832 *International Conference of the IEEE Engineering in Medicine and Biology Society (EMBC)* 222–  
833 225 (2015). doi:10.1109/EMBC.2015.7318340.
- 834 87. Pichardo, S. BabelBrain: An Open-Source Application for Prospective Modeling of Transcranial  
835 Focused Ultrasound for Neuromodulation Applications. *IEEE Transactions on Ultrasonics,*  
836 *Ferroelectrics, and Frequency Control* **70**, 587–599 (2023).
- 837 88. Brainard, D. H. The Psychophysics Toolbox. *Spatial Vis* **10**, 433–436 (1997).
- 838 89. Fahrenfort, J. J., Scholte, H. S. & Lamme, V. A. F. Masking Disrupts Reentrant Processing in  
839 Human Visual Cortex. *Journal of Cognitive Neuroscience* **19**, 1488–1497 (2007).
- 840 90. Rolls, E. T., Tovée, M. J. & Panzeri, S. The Neurophysiology of Backward Visual Masking:  
841 Information Analysis. *Journal of Cognitive Neuroscience* **11**, 300–311 (1999).
- 842 91. Stanislaw, H. & Todorov, N. Calculation of signal detection theory measures. *Behavior Research*  
843 *Methods, Instruments, & Computers* **31**, 137–149 (1999).
- 844 92. Tuzlukov, V. P. *Signal Detection Theory*. (Birkhäuser Boston, Boston, MA, 2001).  
845 doi:10.1007/978-1-4612-0187-8.
- 846 93. Wickens, T. D. *Elementary Signal Detection Theory*. (Oxford Univ. Press, Oxford, 2002).
- 847 94. Macmillan, N. A. & Kaplan, H. L. Detection theory analysis of group data: Estimating sensitivity  
848 from average hit and false-alarm rates. *Psychological Bulletin* **98**, 185–199 (1985).
- 849 95. Smith, S. M. *et al.* Resting-state fMRI in the Human Connectome Project. *NeuroImage* **80**, 144–  
850 168 (2013).
- 851 96. Glasser, M. F. *et al.* The minimal preprocessing pipelines for the Human Connectome Project.  
852 *NeuroImage* **80**, 105–124 (2013).
- 853 97. Schaefer, A. *et al.* Local-Global Parcellation of the Human Cerebral Cortex from Intrinsic  
854 Functional Connectivity MRI. *Cerebral Cortex* **28**, 3095–3114 (2018).
- 855 98. Thomas Yeo, B. T. *et al.* The organization of the human cerebral cortex estimated by intrinsic  
856 functional connectivity. *Journal of Neurophysiology* **106**, 1125–1165 (2011).

857 **ACKNOWLEDGEMENTS**

858 We express our sincere gratitude to our study coordinators, Amy McKinney and Aaron Ellis, for  
859 their invaluable contributions to participant recruitment, meticulous scheduling, and ensuring the  
860 smooth execution of this study. This work was supported by the National Institute of General  
861 Medical Sciences of the National Institutes of Health grants R01GM103894 (to A.G.H. and Z.H.).  
862 The content is solely the responsibility of the author and does not necessarily represent the official  
863 views of the National Institutes of Health.

864

865 **AUTHOR CONTRIBUTIONS STATEMENT**

866 H.J. and Z.H. designed the study and set up the experimental apparatus. H.J. devised the  
867 template rescaling method and developed the code. H.J., P.F., and Z.H. conducted the  
868 experiments. H.J. analyzed the data, prepared the figures, and drafted the manuscript. Z.H. co-  
869 analyzed the data. Z.H., G.A.M. and A.G.H. interpreted the data and edited the manuscript.

870

871 **COMPETING INTERESTS STATEMENT**

872 The authors declare no competing interests.